

# Gaussian Set Surface Reconstruction through Per-Gaussian Optimization

Zhentaο Huang  
University of Guelph  
School of Computer Science  
zhentaο@uoguelph.ca

Di Wu  
University of Macau  
Faculty of Science and Technology  
diwu96063@gmail.com

Zhenbang He  
University of British Columbia Okanagan  
Irving K. Barber Faculty of Science  
zbhe96@student.ubc.ca

Minglun Gong  
University of Guelph  
School of Computer Science  
minglun@uoguelph.ca

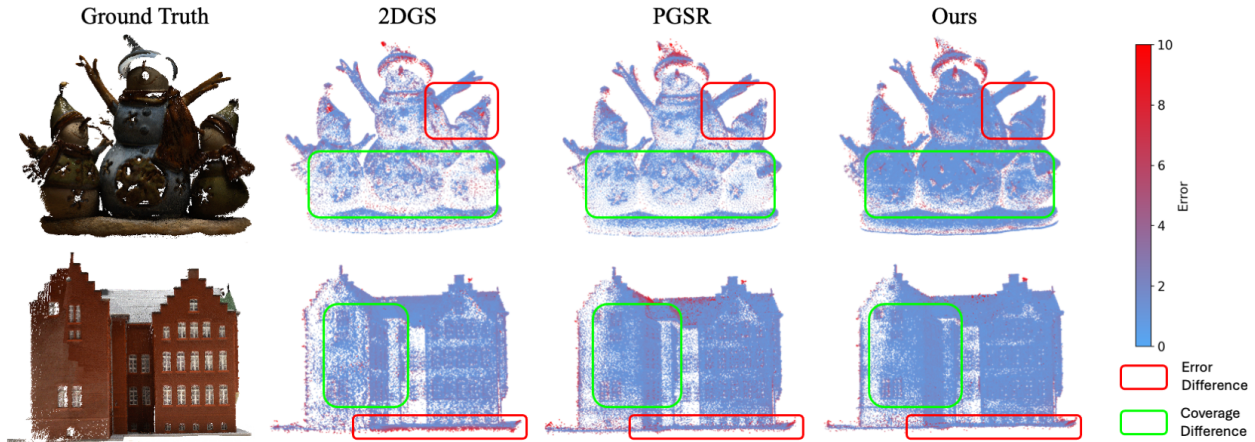


Figure 1. Comparison of 3D Gaussian distributions from 2DGS, PGSR, and our method across two scenes. Gaussian centers are visualized as colored points, with hue indicating surface distance error. Areas where the white background is visible through the Gaussians denote incomplete surface coverage. Red and green boxes highlights regions with improved accuracy and coverage, respectively. Quantitative and visual results confirm that our approach achieves both a lower reconstruction error and a more complete Gaussian representation.

## Abstract

3D Gaussian Splatting (3DGS) effectively synthesizes novel views through its flexible representation, yet fails to accurately reconstruct scene geometry. While modern variants like PGSR introduce additional losses to ensure proper depth and normal maps through Gaussian fusion, they still neglect individual placement optimization. This results in unevenly distributed Gaussians that deviate from the latent surface, complicating both reconstruction refinement and scene editing. Motivated by pioneering work on Point Set Surfaces, we propose Gaussian Set Surface Reconstruction (GSSR), a method designed to distribute Gaussians evenly along the latent surface while aligning their dominant normals with the surface normal. GSSR enforces fine-grained geometric alignment through a combination of

pixel-level and Gaussian-level single-view normal consistency and multi-view photometric consistency, optimizing both local and global perspectives. To further refine the representation, we introduce an opacity regularization loss to eliminate redundant Gaussians and apply periodic depth- and normal-guided Gaussian reinitialization for a cleaner, more uniform spatial distribution. Our reconstruction results demonstrate significantly improved geometric precision in Gaussian placement, enabling intuitive scene editing and efficient generation of novel Gaussian-based 3D environments. Extensive experiments validate GSSR’s effectiveness, showing enhanced geometric accuracy while preserving high-quality rendering performance. **Our code will be released upon acceptance of the paper.**

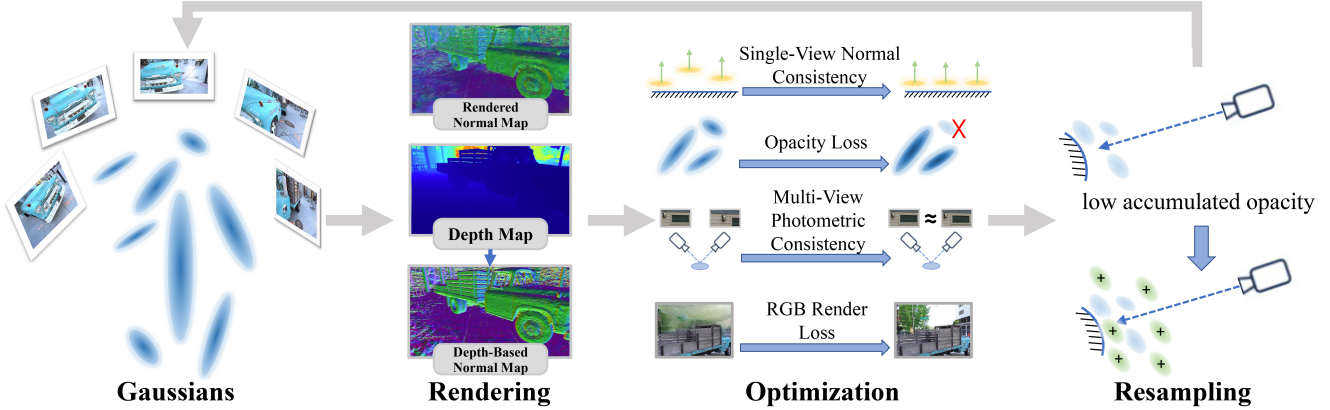


Figure 2. Overview of the proposed GSSR pipeline. Given multi-view posed images and initialized 3D Gaussians, we render the depth map, depth-based normals and alpha-blended normals. The optimization stage includes four major components: (1) single-view normal consistency, (2) multi-view photometric consistency (3) RGB rendering loss, and (4) opacity regularization. Additionally, Gaussians are periodically resampled using our view-based opacity-guided strategy, resulting in a more uniform and accurate distribution.

## 1. Introduction

Novel View Synthesis (NVS) remains a fundamental challenge in computer vision and graphics, enabling photorealistic scene rendering from sparse inputs for applications ranging from eXtended Reality (XR) to autonomous systems. Modern NVS approaches can be broadly categorized by their treatment of scene geometry: explicit modeling methods that reconstruct accurate 3D surfaces [27, 28] and implicit scene representations that bypass explicit reconstruction [21, 23, 25].

With advances in deep neural networks, research on implicit scene representations has gained momentum. In particular, Neural Radiance Fields (NeRF) [25] leverages MLPs to model scenes volumetrically, achieving unprecedented rendering quality. However, these methods incur significant costs: slow training, high computational demands, and limited editability.

3D Gaussian Splatting [21] overcomes these limitations through its explicit, Gaussian-based representation. By employing differentiable rasterization of 3D Gaussians, it achieves real-time rendering while maintaining NeRF-comparable visual quality. The discrete nature of Gaussians offers advantages in scene manipulation and surface reconstruction compared to continuous implicit representations. However, standard 3DGS prioritizes rendering quality over geometric precision, often producing misaligned Gaussian distributions that poorly approximate physical surfaces. Recent extensions like 2DGS [15], PGSR [3], and GauSurf [30] address this through geometric regularization, optimizing Gaussians to produce accurate depth and normal maps. While these methods improve surface estimation, they focus on aggregate outputs rather than individual Gaussian placement. Consequently, the Gaussians remain unevenly

distributed and misaligned with underlying surfaces, limiting their effectiveness for geometry-sensitive applications including scene editing and dynamic object deformation.

Inspired by the foundational work on Point Set Surfaces [1], we propose Gaussian Set Surface Reconstruction (GSSR), a method that optimizes Gaussian distributions by: (1) anchoring centers to latent scene surfaces, (2) enforcing spatial uniformity, and (3) aligning dominant normals with surface geometry. GSSR’s explicit geometric formulation enables direct compatibility with point-based manipulation techniques, opening new possibilities for precise scene editing, animation workflows, and dynamic scene processing – effectively bridging the gap between neural rendering quality and practical 3D content creation needs.

GSSR optimizes individual Gaussian location and orientation through two key mechanisms: (1) The application of explicit geometric constraints derived from estimated planar structures and surface smoothness, encouraging Gaussians to coalesce onto latent scene surfaces; and (2) A joint optimization of opacity and position coupled with adaptive pruning, which aggressively eliminates Gaussians with low contributions while strategically repositioning others at underrepresented areas. Our experiments across multiple datasets demonstrate that our approach yields a cleaner scene representation with more geometrically consistent ellipsoids while preserving high rendering quality.

In summary, our key contributions include:

- GSSR, a 3DGS framework optimizing Gaussians for uniform placement and precise surface alignment
- A geometric regularization technique that advances beyond prior 3DGS methods in per-Gaussian depth/normal accuracy and visual coherence

- An opacity-position optimization strategy that prunes redundancies while enforcing surface adherence
- State-of-the-art Gaussian accuracy and completeness across three datasets, without rendering quality loss

## 2. Related Work

### 2.1. Gaussian Splatting for 3D Reconstruction

Due to the explicit Gaussian ellipsoids representation of 3DGS, many effective works [3, 5, 8, 13, 15, 29, 30, 33] that focus on applying geometric regularization to improve geometry accuracy are proposed. SuGaR [13] introduces a signed distance function and density supervision to guide Gaussians toward object surfaces. 2DGS [15] replaces volumetric ellipsoids with the elliptical disk-shaped Gaussians, which better align with local geometry and improve surface fidelity during rendering. GOF [34] integrates implicit neural representation within the Gaussian framework to enhance geometric detail and multi-view consistency. PGSR [3] introduces a depth estimation strategy and geometric constraints that yield smoother and more accurate surface reconstruction. GausSurf [30] incorporates geometric guidance by combining patch-match MVS for texture-rich regions and normal priors for texture-less areas. Additionally, methods like GSDF [33] and NeuSG [4] combine 3DGS with Signed Distance Field (SDF) networks to improve reconstruction quality. While these approaches effectively improve surface smoothness and depth accuracy, they often result in overly dense and irregular Gaussian distributions. In contrast, our method not only enhances surface reconstruction but also produces a cleaner and more spatially consistent Gaussian representation, while maintaining high-fidelity rendering quality.

### 2.2. Scene Editing

3D Gaussian Splatting offers photorealistic rendering and holds great promise for applications in XR, content creation, and digital twins. However, its ellipsoidal representation lacks geometric consistency with real-world surfaces, making intuitive and semantically meaningful scene editing difficult compared to mesh-based approaches. Recent methods such as GaussianEditor [6], Gaussian Grouping [32], Point’n Move [16], and Feng et al. [9] explore 3DGS editing through semantic prompts, mask-based grouping, or improved Gaussian splitting, but are largely limited to basic object-level operations such as removal, rotation, and translation. In parallel, some efforts have explored scene editing in NeRF-based representations [14, 17, 31, 35], addressing similar challenges of geometry-awareness and user interaction. While promising, these approaches still face limitations due to implicit nature of NeRF and the lack of controllable structure. In this work, we aim to align the generated 3D Gaussians as closely as possible with the physical

surfaces, thereby enhancing geometric consistency and enabling more reliable and flexible editing in 3DGS representations.

## 3. 3D Gaussian Splatting Preliminaries

3D Gaussian Splatting builds on Elliptical Weighted Average (EWA) splatting [36], extended with a differentiable formulation [21] to optimize both the number and parameters of Gaussians for scene representation. Each Gaussian is defined by its center  $\mathbf{x} \in \mathbb{R}^3$ , opacity  $\alpha \in [0, 1]$ , covariance matrix in world space  $\Sigma_i \in \mathbb{R}^{3 \times 3}$ , and view-dependent color via 16 SH coefficients. During rendering, the final pixel color  $C$  is computed by compositing  $N$  depth-sorted 2D Gaussians:

$$C(\mathbf{p}) = \sum_{i=1}^N T_i \alpha_i \mathbf{c}_i, \quad T_i = \prod_{j=1}^{i-1} (1 - \alpha_j \mathcal{G}_j^{2D}(\mathbf{p})) \quad (1)$$

where  $\mathbf{c}_i$  represents the view-dependent color, and  $\mathcal{G}_j^{2D}$  is the projected 2D Gaussian distribution. To render depth, previous methods [7, 20] replace  $\mathbf{c}_i$  with the Gaussian center depth  $z_i$  in Equation 1. However, this yields biased, curved surfaces. Following PGSR [3], we instead computed unbiased depth using Gaussian surface normals  $\mathbf{n}_i$ , aligned with the minimum scale axis. The per-Gaussian tangent plane distance is:

$$d_i = (R_c^\top (\boldsymbol{\mu}_i - \mathbf{t}_c))^\top R_c^\top \mathbf{n}_i, \quad (2)$$

where  $R_c$  is the world-to-camera rotation and  $\mathbf{t}_c$  is the camera origin. The global depth is then computed via ray-plane intersection:

$$D(\mathbf{p}) = \frac{d(\mathbf{p})}{\mathbf{N}(\mathbf{p})^\top K^{-1} \tilde{\mathbf{p}}}, \quad (3)$$

with  $K$  the intrinsic matrix and  $\tilde{\mathbf{p}}$  the homogeneous pixel coordinate. This formulation ensures geometry-consistent depth estimation independent of Gaussian density.

## 4. Methodology

Given posed input images, we reconstruct a Gaussian Set Surface (GSS) – a collection of Gaussians that are uniformly distributed and precisely aligned with underlying scene surfaces. This representation combines the geometric manipulability of Point Set Surfaces [1] with 3DGS’s strengths in photorealistic novel view synthesis. Our Gaussian Set Surface reconstruction pipeline consists of three key components: (1) geometric regularization for accurate depth and normal estimation, (2) per-Gaussian optimization to refine individual geometric properties, and (3) enhanced density control enforcing uniform spatial distribution.

## 4.1. Geometric Regularization

### 4.1.1 Flattening 3D Gaussian

Accurately capturing real-world scene geometry using 3D Gaussians is inherently challenging. To better align with the true surface structure, the Gaussians are instead flattened into 2D representations, allowing them to more precisely conform to the underlying geometry of the scene. Rather than initializing with 2D Gaussian Splatting (2DGS) [15], a scale loss  $L_s$  is introduced to progressively compress each Gaussian ellipsoid along its smallest scale axis. This process effectively flattens the ellipsoid into a plane that best approximates the underlying surface geometry. Following the approach in [3, 4], a penalty is applied directly to the minimum scale of each Gaussian to enforce flattening:

$$\mathcal{L}_s = \|\min(s_1, s_2, s_3)\|_1, \quad (4)$$

where  $s_1, s_2, s_3$  represents the scale parameters of each Gaussian ellipsoid.

### 4.1.2 Single-View Normal Consistency

As illustrated in Figure 3 (a), a locally discontinuous Gaussian-rendered plane may exhibit a smooth normal field, leading to inconsistency between local surface normals and depth geometry. To address this issue, encouraged by prior works [5, 12, 20, 29], a single-view normal loss is introduced to enforce local geometric consistency for every pixel  $p$  in the image domain  $\Omega$ :

$$\mathcal{L}_{\text{normal}} = \frac{1}{\Omega} \sum_{p \in \Omega} \|\mathbf{n}_{\text{depth}}(p) - \mathbf{n}_{\text{rendered}}(p)\|_1, \quad (5)$$

where  $\mathbf{n}_{\text{depth}}(p)$  denotes the surface normal estimated from depth gradients of neighboring pixels, and  $\mathbf{n}_{\text{rendered}}(p)$  denotes the normal rendered from the Gaussian sets.

### 4.1.3 Multi-View Photometric Consistency

Photometric consistency is a widely used supervision signal in Multi-View Stereo (MVS) frameworks, leveraging color similarity across views to constrain geometry [10, 11, 18]. Among various formulations, the Normalized Cross-Correlation (NCC) metric is particularly robust to illumination variation and exposure differences. In this work, the photometric NCC loss is adopted to enforce multi-view consistency by comparing image patches in neighboring views. For each pixel  $p_r$  in the reference view, the corresponding pixel  $p_n$  in a neighboring view is computed using a plane-induced homography:

$$p_n = H_{rn} \cdot p_r, \quad (6)$$

$$H_{rn} = K \left( R_{rn} - \frac{\mathbf{T}_{rn} \mathbf{n}_r^\top}{d_r} \right) K_r^{-1}, \quad (7)$$

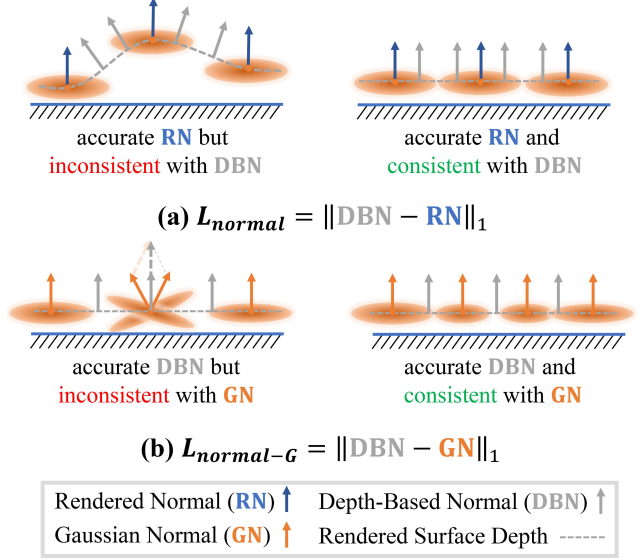


Figure 3. Illustration of (a)  $L_{\text{normal}}$  and (b)  $L_{\text{normal-G}}$ . **Gaussian Normal** is derived from the direction of the Gaussian’s minimum scale axis. **Rendered Normal** is computed via alpha blending of Gaussian normals along each pixel ray. **Depth-Based Normal** is estimated from the depth gradients of neighboring pixels.

where  $R_{rn}$  and  $T_{rn}$  denote the relative rotation and translation from the reference view to the neighboring view, and  $\mathbf{n}_r, d_r$  are the rendered surface normal and plane distance, respectively. As illustrated in Figure 4 (a), after computing the corresponding patch in the neighboring view, we followed the forward and backward projection error weighted NCC loss in PGSR [3]:

$$\phi(p_r) = \|\mathbf{p}_r - H_{nr} H_{rn} \mathbf{p}_r\| \quad (8)$$

$$w(p_r) = \begin{cases} \frac{1}{\exp(\phi(p_r))}, & \text{if } \phi(p_r) < 1 \\ 0, & \text{if } \phi(p_r) \geq 1 \end{cases} \quad (9)$$

$$\mathcal{L}_{\text{mv}} = \frac{1}{\Omega} \sum_{p_r \in \Omega} w(p_r) (1 - \text{NCC}(\mathbf{I}_r(p_r), \mathbf{I}_n(H_{rn} \mathbf{p}_r))), \quad (10)$$

where  $\phi(p_r)$  represents the forward and backward projection error. If this error exceeds a predefined threshold, the pixel is considered occluded or associated with significant geometric inconsistency.

## 4.2. Instance-Level Gaussian Optimization

Although geometric regularization enforces scene-level accuracy, it often fails to achieve satisfactory instance-level accuracy. Specifically, the Gaussians tend to form a thick layer surrounding the actual object surface, as illustrated

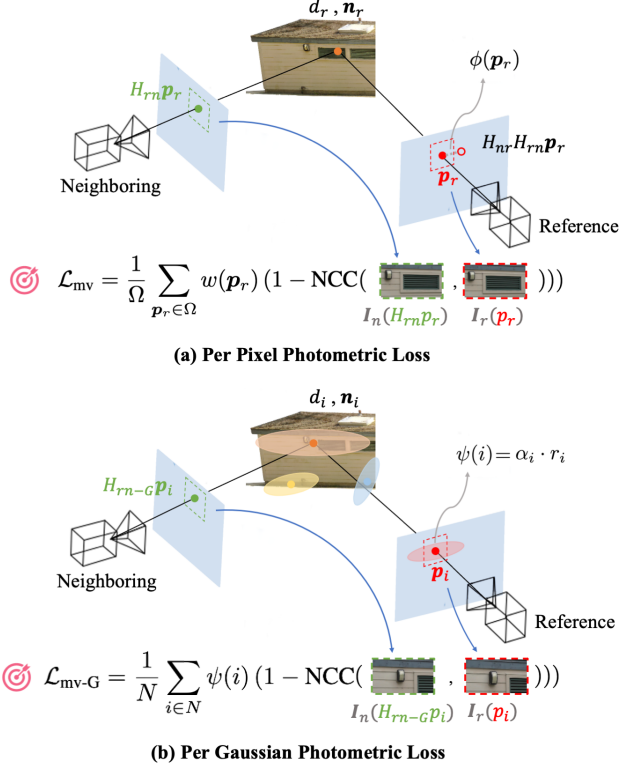


Figure 4. Illustration of pixel-level (a) and Gaussian-level (b) multi-view photometric loss.

in Figure 5. This is primarily because the pixel-level geometric loss only constrains the alpha-blended depth and normal, without explicitly supervising individual Gaussian ellipsoids. To address this issue, we further incorporate geometric constraints to enforce single-view normal consistency and multi-view photometric consistency on each Gaussian instance. To filter out occluded Gaussians, we select only those whose center depth lies in front of the rendered depth map within a predefined tolerance for each training view.

#### 4.2.1 Bilaterally Weighted Normal Loss

To enforce the single-view normal loss, a penalty is applied to the difference between each filtered Gaussian’s normal and its depth-inferred normal at the center pixel. However, directly adding this loss can introduce instability during optimization, especially in the presence of incorrect, near-transparent, or very small Gaussians. To mitigate this issue, we adopt a bilaterally weighted normal loss, where the weights are determined by each Gaussian’s opacity and splat size:

$$\mathcal{L}_{\text{normal-G}} = \frac{1}{N} \sum_{i=1}^N \psi(i) \|\mathbf{n}_{\text{depth}}(\mathbf{p}_i) - \mathbf{n}_i\|_1, \quad (11)$$

$$\psi(i) = \alpha_i \cdot r_i, \quad (12)$$

where  $\mathbf{p}_i$  denotes the 2D pixel location obtained by projecting the 3D center of the  $i^{\text{th}}$  Gaussian onto the image plane,  $\mathbf{n}_i$  is the Gaussian’s normal in camera space, and  $\psi(i)$  is a visibility-based weight defined as the product of opacity  $\alpha_i$  and the projected splat radius  $r_i$ .

#### 4.2.2 Bilaterally Weighted Photometric Loss

As illustrated in Figure 4 (b), the photometric NCC loss is employed to enforce multi-view consistency by comparing local image patches sampled around the projected centers of depth-filtered Gaussians. The same bilateral weight  $\psi$  is applied to each Gaussian instance filtered by depth.

$$H_{rn-G} = K \left( R_{rn} - \frac{\mathbf{T}_{rn} \mathbf{n}_i^\top}{d_i} \right) K_r^{-1}, \quad (13)$$

$$\mathcal{L}_{mv-G} = \frac{1}{N} \sum_{i \in N} \psi(i) (1 - \text{NCC}(I_r(\mathbf{p}_i), I_n(H_{rn-G} \cdot \mathbf{p}_i))), \quad (14)$$

This loss encourages the reconstructed geometry to align with photometrically consistent regions across views, thereby improving the geometric accuracy of individual Gaussian instances.

#### 4.3. Gaussian Density Control

In this framework, the original gradient-based Gaussian densification scheme from 3DGS is retained, while an additional opacity loss and Gaussian resampling strategy are introduced to perform density control.

##### 4.3.1 Depth Filtered Opacity Loss

One major reason that Gaussians form a thick layer surrounding the actual object surface is that many of them remain semi-transparent. To address this issue, we introduce an opacity regularization loss that encourages each Gaussian’s opacity to converge toward either 0 (fully transparent and removable) or 1 (fully opaque):

$$\mathcal{L}_{\text{opacity}} = \frac{1}{N} \sum_{i=1}^N (\log \alpha_i + \log(1 - \alpha_i)), \quad (15)$$

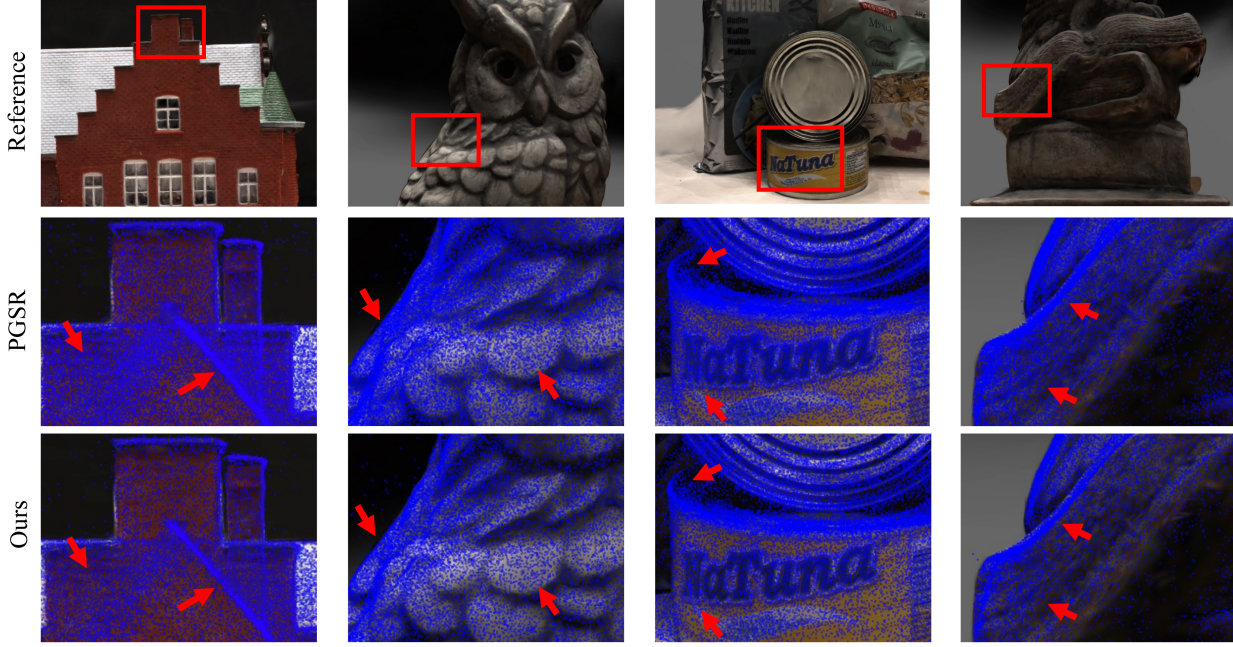


Figure 5. Comparison of Gaussian density distribution between PGSR and our method. Our approach produces lower Gaussian density, especially on planar regions (see red arrows), where the splats are more compact and narrowly distributed, demonstrating better geometric compactness and representation efficiency.

Table 1. Top: Reconstruction on DTU (Chamfer Distance  $\downarrow$ ). Middle: Reconstruction on DTU (Accuracy of Gaussian Centroid  $\downarrow$ ). Bottom: Reconstruction on DTU (Completeness of Gaussian  $\downarrow$ ). Red, orange and yellow backgrounds denote the best, second-best, and third-best results respectively.

	24	37	40	55	63	65	69	83	97	105	106	110	114	118	122	Mean
2DGS* [15]	0.49	0.79	0.34	0.42	0.95	0.95	0.83	1.25	1.24	0.64	0.62	1.34	0.44	0.69	0.48	0.76
GOF* [34]	0.49	0.83	0.36	0.38	1.33	0.87	0.73	1.24	1.32	0.66	0.73	1.26	0.52	0.82	0.51	0.80
PGSR* [3]	0.34	0.55	0.39	0.35	0.78	0.58	0.49	1.09	0.63	0.59	0.47	0.50	0.30	0.37	0.34	0.52
GausSurf† [30]	0.35	0.55	0.34	0.34	0.77	0.58	0.51	1.10	0.69	0.60	0.43	0.49	0.32	0.40	0.37	0.52
Ours	0.33	0.57	0.37	0.33	0.78	0.62	0.51	1.11	0.68	0.59	0.48	0.55	0.30	0.38	0.35	0.53
2DGS*	0.66	1.02	0.55	0.60	0.88	1.03	0.92	0.55	0.95	0.47	0.52	0.99	0.63	0.42	0.41	0.71
GOF*	0.98	1.28	0.99	0.85	1.11	1.29	1.08	0.77	1.10	0.62	0.65	1.05	0.79	0.48	0.61	0.91
PGSR*	0.58	0.68	0.85	0.71	0.74	0.64	0.68	0.51	0.74	0.45	0.46	0.60	0.46	0.37	0.37	0.59
Ours	0.32	0.47	0.46	0.29	0.56	0.42	0.39	0.43	0.52	0.33	0.26	0.33	0.21	0.26	0.25	0.37
2DGS*	0.92	0.87	1.02	0.72	1.06	1.47	1.25	1.94	1.70	1.11	1.56	1.51	0.81	1.33	1.09	1.22
GOF*	0.71	0.72	0.81	0.59	0.96	1.33	1.12	1.78	1.70	0.99	1.38	1.14	0.69	1.19	0.92	1.07
PGSR*	0.75	0.72	0.88	0.64	0.82	1.16	0.97	1.69	1.44	0.96	1.30	0.90	0.68	1.05	0.86	0.99
Ours	0.62	0.61	0.58	0.51	0.56	0.88	0.67	1.52	1.17	0.82	0.85	0.54	0.46	0.64	0.55	0.73

\* Reproduced results using the authors' official implementation.

† The source code is not available; only mesh-based evaluation results are reported.

#### 4.3.2 Depth & Normal Reinitialization

To adaptively control the spatial distribution of Gaussians, we introduce a view-based, opacity-guided resampling strategy executed every fixed number of iterations. For each training view, the accumulated opacity  $\alpha_{acc}$  is computed by rendering all Gaussians located in front of the rendered depth map. The sampling weight at each pixel  $p$  is

defined as the inverse transmittance:  $1 - \alpha_{acc}(p)$ . The number of newly sampled Gaussians for the view is determined by:

$$N_{\text{new}} = N_{\text{per-view}} \cdot \frac{1}{|\Omega|} \sum_{p \in \Omega} (1 - \alpha_{acc}(p)), \quad (16)$$

where  $N_{\text{per-view}}$  is a predefined constant that controls the base number of Gaussians sampled per view. To prioritize

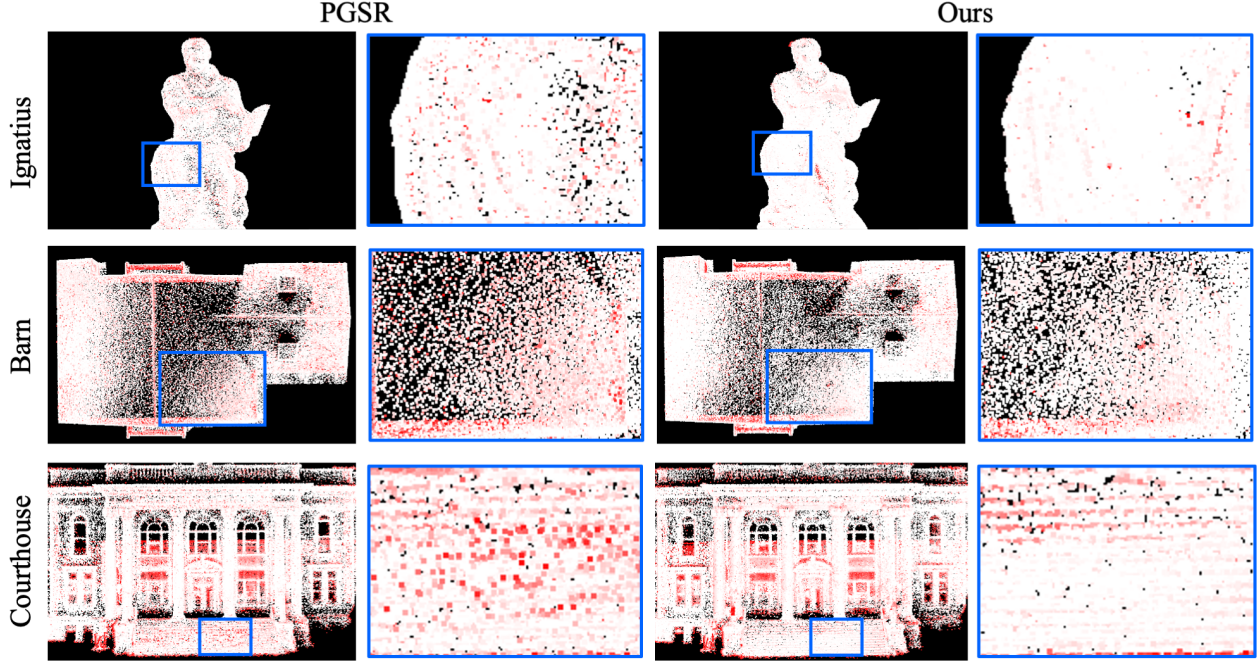


Figure 6. Comparison of Gaussian centroid precision on TnT. **Less red points** in reconstructed scenes indicate **higher accuracy**.

Table 2. Top: Reconstruction on TnT (F1 Score  $\uparrow$ ). Middle: Reconstruction on TnT (Precision of Gaussian Centroid  $\uparrow$ ). Bottom: Reconstruction on TnT (Completeness of Gaussian  $\uparrow$ ).

	Barn	Caterpillar	Courthouse	Ignatius	Meetingroom	Truck	Mean
2DGS <sup>+</sup> [15]	0.46	0.24	0.15	0.49	0.19	0.45	0.33
GOF <sup>+</sup> [34]	0.55	0.39	0.28	0.71	0.26	0.57	0.46
PGSR <sup>+</sup> [3]	0.65	0.45	0.21	0.81	0.33	0.62	0.51
GausSurf <sup>+</sup> [30]	0.50	0.42	0.30	0.73	0.39	0.65	0.50
Ours	0.64	0.42	0.22	0.80	0.32	0.59	0.50
2DGS <sup>+</sup>	0.65	0.59	0.62	0.71	0.47	0.71	0.62
GOF <sup>+</sup>	0.65	0.60	0.62	0.77	0.49	0.70	0.64
PGSR <sup>+</sup>	0.63	0.58	0.56	0.70	0.49	0.69	0.61
Ours	0.66	0.66	0.52	0.83	0.47	0.78	0.65
2DGS <sup>+</sup>	0.08	0.07	0.04	0.09	0.04	0.11	0.07
GOF <sup>+</sup>	0.12	0.09	0.05	0.15	0.05	0.16	0.10
PGSR <sup>+</sup>	0.16	0.13	0.08	0.16	0.09	0.20	0.14
Ours	0.20	0.19	0.08	0.28	0.07	0.32	0.19

under-represented regions, 3D points are drawn from the rendered point cloud via multinomial sampling, with probabilities proportional to the sampling weights. For each selected point, its 3D position and normal are extracted from the rendered depth and normal maps, and then transformed to world coordinates. To enhance robustness, a bilateral filter is applied to the depth and normal maps, incorporating both spatial proximity and value similarity. New Gaussians are initialized at these sampled points and flattened according to the corresponding normals.

## 5. Experiments

This section presents an evaluation of the proposed method, including implementation details and ablation studies. **The source code will be released upon the acceptance of the paper.**

### 5.1. Datasets

We evaluate our method on three datasets: DTU [19], Tanks and Temples (TnT) [22] and Mip-NeRF360 [2], covering both indoor and outdoor environments. The DTU dataset consists of 124 sets of high-quality images of various objects with complex geometries and textures, captured under controlled lighting with camera poses. The Tanks and Temples dataset serves as a benchmark for complex large-scale scene reconstruction using high-resolution video input. Following PGSR [3], we evaluate 3D reconstruction performance on 15 DTU scenes and 6 Tanks and Temples scenes. To assess novel view synthesis, we use the Mip-NeRF360 dataset, which contains high-resolution images of unbounded outdoor scenes.

### 5.2. Implementation Details

The implementation of our method is based on PyTorch. All experiments are conducted on a desktop equipped with an NVIDIA RTX 4090 GPU. Our training strategy and hyperparameters are generally consistent with previous works 3DGS [21] and PGSR [3]. All scenes are trained for 30,000 iterations. The final training loss is defined as:

Table 3. Quantitative results on the Mip-NeRF360 [2] dataset.

Method	Indoor scenes			Outdoor scenes			Average on all scenes		
	PSNR $\uparrow$	SSIM $\uparrow$	LPIPS $\downarrow$	PSNR $\uparrow$	SSIM $\uparrow$	LPIPS $\downarrow$	PSNR $\uparrow$	SSIM $\uparrow$	LPIPS $\downarrow$
2DGS [15]	30.40	0.916	0.195	24.34	0.717	0.246	27.37	0.817	0.221
GOF [34]	30.79	0.924	0.184	24.82	0.750	0.202	27.81	0.837	0.193
PGSR* [3]	30.20	0.930	0.158	24.77	0.752	0.204	27.49	0.841	0.181
GausSurf [30]	30.05	0.920	0.183	25.09	0.753	0.212	27.57	0.837	0.198
Ours	29.79	0.924	0.168	24.47	0.724	0.250	27.13	0.824	0.209

Table 4. Ablation study on DTU.

Method	Chamfer Distance $\downarrow$	Precision $\downarrow$	Completeness $\downarrow$
w/o Resampling	0.57	0.48	0.92
w/o $L_{normal}$	0.53	0.40	0.68
w/o $L_{normal-G}$	0.54	0.39	0.74
w/o $L_{mv}$	0.63	0.43	0.85
w/o $L_{mv-G}$	0.51	0.47	0.73
Full model	0.53	0.37	0.73

$$\mathcal{L} = \mathcal{L}_{RGB} + \lambda_1 \mathcal{L}_{normal} + \lambda_2 \mathcal{L}_{normal-G} + \lambda_3 \mathcal{L}_{opacity} + \lambda_4 \mathcal{L}_{mv} + \lambda_5 \mathcal{L}_{mv-G}. \quad (17)$$

We set the weights as follows:  $\lambda_1 = 0.015$ ,  $\lambda_2 = 0.0075$ ,  $\lambda_3 = 0.0001$ ,  $\lambda_4 = 0.15$ , and  $\lambda_5 = 0.15$ . Depth and normal reinitialization are performed at iterations 5,000 and 10,000. We set the number of Gaussian sampled per-view  $N_{per-view} = 10,000$ .

### 5.3. Results

**Reconstruction:** To assess overall reconstruction accuracy, we use the F1 score on the Tanks and Temples dataset and the Chamfer Distance on the DTU dataset. We compare the reconstruction performance of GSSR against recent GS-based methods, including 2DGS [15], GOF [34], PGSR [3], GausSurf [30]. For evaluation, we first render a depth map from each training view and then apply Truncated Signed Distance Function (TSDF) Fusion [26] to integrate them into a unified TSDF field. A mesh is subsequently extracted using the Marching Cube algorithm [24], which is used to compute the reconstruction metrics. As shown in the top rows of Tables 1 and 2, our method achieves performance comparable to state-of-the-art results on both datasets.

**Gaussian Instance Accuracy:** To assess the geometric fidelity of individual Gaussians, we report accuracy (average point-to-ground-truth distance) and completeness (average ground-truth-to-point distance) as the two components of Chamfer Distance on the DTU dataset. Similarly, we report precision and recall as components of the F1 score for the Tanks and Temples dataset. As shown in Table 1 and Table 2, GSSR consistently outperforms all other methods in Gaussian-level geometric quality. Figure 1 provides a visual comparison on the DTU dataset between GSSR, 2DGS [15], and PGSR [3], where GSSR yields both lower position error and more complete coverage. Figure 6 shows Gaussian center precision across three Tanks and Temples scenes, demonstrating GSSR’s higher accuracy. Figure 5 visualizes the spatial density of Gaussians, where GSSR produces a more uniform distribution and thinner layers aligned with object surfaces.

**Novel View Synthesis:** To evaluate novel view synthesis quality, we follow the experimental setup of 3DGS [21] and

conduct validation on the Mip-NeRF360 dataset [2]. Our method is compared against several GS-based approaches. As shown in Table 3, the proposed framework not only achieves a strong surface reconstruction performance, but also delivers competitive results in novel view rendering.

### 5.4. Ablation Study

To further evaluate the effectiveness of key components in our proposed method, we perform ablation studies on the DTU dataset. We report the quality of the reconstructed mesh, as well as the accuracy and completeness of the Gaussian centers. Detailed quantitative results for each ablated variant are presented in Table 4. The resampling strategy plays a critical role in improving completeness by reducing under-coverage. Loss terms  $\mathcal{L}_{normal}$ ,  $\mathcal{L}_{normal-G}$ , and  $\mathcal{L}_{mv-G}$  significantly enhance Gaussian instance accuracy, while the multi-view consistency loss  $\mathcal{L}_{mv}$  is crucial for improving overall geometric quality. Overall, the full model consistently achieves the best trade-off across all metrics, demonstrating the importance of each component in enhancing geometric fidelity and scene coverage.

## 6. Conclusion

We present Gaussian Set Surface Reconstruction (GSSR), a novel approach inspired by Point Set Surfaces [1] that represents scenes using dense, geometrically-precise 3D Gaussians with uniform spatial distribution. GSSR enforces geometric accuracy through multi-scale constraints (pixel-level and Gaussian-level) while preserving photorealistic rendering capabilities. Our framework introduces: (1) an opacity regularization loss to prune redundant Gaussians, and (2) a view-adaptive resampling strategy for optimal spatial distribution. Comprehensive evaluation across three real-world datasets demonstrates GSSR’s superior ge-

ometric consistency and rendering fidelity compared to state-of-the-art 3DGS methods, producing cleaner distributions that better adhere to scene geometry.

**Limitation:** While GSSR significantly improves per-Gaussian accuracy, two limitations remain: First, these gains do not directly translate to improved mesh reconstruction or alpha-blended depth quality. Second, the view-based Gaussian sampling requires empirical parameter setting, though this provides coarse control over Gaussian density. Future work will investigate adaptive sampling strategies to automate this process.

## References

- [1] M. Alexa, J. Behr, D. Cohen-Or, S. Fleishman, D. Levin, and C.T. Silva. Point set surfaces. In *Proceedings Visualization, 2001. VIS '01.*, pages 21–29, 537, 2001. 2, 3, 8
- [2] Jonathan T Barron, Ben Mildenhall, Dor Verbin, Pratul P Srinivasan, and Peter Hedman. Mip-nerf 360: Unbounded anti-aliased neural radiance fields. In *Proceedings of the IEEE/CVF conference on computer vision and pattern recognition*, pages 5470–5479, 2022. 7, 8
- [3] Danpeng Chen, Hai Li, Weicai Ye, Yifan Wang, Weijian Xie, Shangjin Zhai, Nan Wang, Haomin Liu, Hujun Bao, and Guofeng Zhang. Pgsr: Planar-based gaussian splatting for efficient and high-fidelity surface reconstruction. *IEEE Transactions on Visualization and Computer Graphics*, 2024. 2, 3, 4, 6, 7, 8
- [4] Hanlin Chen, Chen Li, and Gim Hee Lee. Neusg: Neural implicit surface reconstruction with 3d gaussian splatting guidance. *arXiv preprint arXiv:2312.00846*, 2023. 3, 4
- [5] Hanlin Chen, Fangyin Wei, Chen Li, Tianxin Huang, Yunsong Wang, and Gim Hee Lee. Vcr-gaus: View consistent depth-normal regularizer for gaussian surface reconstruction. *Advances in Neural Information Processing Systems*, 37:139725–139750, 2024. 3, 4
- [6] Yiwen Chen, Zilong Chen, Chi Zhang, Feng Wang, Xiaofeng Yang, Yikai Wang, Zhongang Cai, Lei Yang, Huaping Liu, and Guosheng Lin. Gaussianeditor: Swift and controllable 3d editing with gaussian splatting. In *Proceedings of the IEEE/CVF conference on computer vision and pattern recognition*, pages 21476–21485, 2024. 3
- [7] Kai Cheng, Xiaoxiao Long, Kaizhi Yang, Yao Yao, Wei Yin, Yuexin Ma, Wenping Wang, and Xuejin Chen. Gaussianpro: 3d gaussian splatting with progressive propagation. In *Forty-first International Conference on Machine Learning*, 2024. 3
- [8] Lue Fan, Yuxue Yang, Minxing Li, Hongsheng Li, and Zhaoxiang Zhang. Trim 3d gaussian splatting for accurate geometry representation. *arXiv preprint arXiv:2406.07499*, 2024. 3
- [9] Qiyuan Feng, Gengchen Cao, Haoxiang Chen, Tai-Jiang Mu, Ralph R. Martin, and Shi-Min Hu. A new split algorithm for 3d gaussian splatting, 2024. 3
- [10] Qiancheng Fu, Qingshan Xu, Yew Soon Ong, and Wenbing Tao. Geo-neus: Geometry-consistent neural implicit surfaces learning for multi-view reconstruction. *Advances in Neural Information Processing Systems*, 35:3403–3416, 2022. 4
- [11] Silvano Galliani, Katrin Lasinger, and Konrad Schindler. Gipuma: Massively parallel multi-view stereo reconstruction. *Publikationen der Deutschen Gesellschaft für Photogrammetrie, Fernerkundung und Geoinformation e. V.*, 25(361-369):2, 2016. 4
- [12] Jian Gao, Chun Gu, Youtian Lin, Zhihao Li, Hao Zhu, Xun Cao, Li Zhang, and Yao Yao. Relightable 3d gaussians: Realistic point cloud relighting with brdf decomposition and ray tracing. In *European Conference on Computer Vision*, pages 73–89. Springer, 2024. 4
- [13] Antoine Guédon and Vincent Lepetit. Sugar: Surface-aligned gaussian splatting for efficient 3d mesh reconstruction and high-quality mesh rendering. In *Proceedings of the IEEE/CVF Conference on Computer Vision and Pattern Recognition*, pages 5354–5363, 2024. 3
- [14] Ayaan Haque, Matthew Tancik, Alexei A Efros, Aleksander Holynski, and Angjoo Kanazawa. Instruct-nerf2nerf: Editing 3d scenes with instructions. In *Proceedings of the IEEE/CVF international conference on computer vision*, pages 19740–19750, 2023. 3
- [15] Binbin Huang, Zehao Yu, Anpei Chen, Andreas Geiger, and Shenghua Gao. 2d gaussian splatting for geometrically accurate radiance fields. In *ACM SIGGRAPH 2024 conference papers*, pages 1–11, 2024. 2, 3, 4, 6, 7, 8
- [16] Jiajun Huang, Hongchuan Yu, Jianjun Zhang, and Hammadi Nait-Charif. Point’n move: Interactive scene object manipulation on gaussian splatting radiance fields. *IET Image Processing*, 18:3507–3517, 07 2024. 3
- [17] Zhentao Huang, Yukun Shi, Neil Bruce, and Minglun Gong. Seald-nerf: Interactive pixel-level editing for dynamic scenes by neural radiance fields. *arXiv preprint arXiv:2402.13510*, 2024. 3
- [18] Zhentao Huang, Yukun Shi, and Minglun Gong. Visibility-aware pixelwise view selection for multi-view stereo matching. In *International Conference on Pattern Recognition*, pages 130–144. Springer, 2025. 4
- [19] Rasmus Jensen, Anders Dahl, George Vogiatzis, Engil Tola, and Henrik Aanæs. Large scale multi-view stereopsis evaluation. In *2014 IEEE Conference on Computer Vision and Pattern Recognition*, pages 406–413. IEEE, 2014. 7
- [20] Yingwenqi Jiang, Jiadong Tu, Yuan Liu, Xifeng Gao, Xiaoxiao Long, Wenping Wang, and Yuexin Ma. Gaussian-shader: 3d gaussian splatting with shading functions for reflective surfaces. In *Proceedings of the IEEE/CVF Conference on Computer Vision and Pattern Recognition*, pages 5322–5332, 2024. 3, 4
- [21] Bernhard Kerbl, Georgios Kopanas, Thomas Leimkühler, and George Drettakis. 3d gaussian splatting for real-time radiance field rendering. *ACM Transactions on Graphics*, 42(4):1–14, 2023. 2, 3, 7, 8
- [22] Arno Knapitsch, Jaesik Park, Qian-Yi Zhou, and Vladlen Koltun. Tanks and temples: Benchmarking large-scale scene reconstruction. *ACM Transactions on Graphics (ToG)*, 36(4):1–13, 2017. 7
- [23] Marc Levoy and Pat Hanrahan. Light field rendering. In *Proceedings of the 23rd Annual Conference on Computer*

- Graphics and Interactive Techniques*, SIGGRAPH '96, page 31–42, New York, NY, USA, 1996. Association for Computing Machinery. 2
- [24] William E Lorensen and Harvey E Cline. Marching cubes: A high resolution 3d surface construction algorithm. In *Seminal graphics: pioneering efforts that shaped the field*, pages 347–353. 1998. 8
- [25] Ben Mildenhall, Pratul P Srinivasan, Matthew Tancik, Jonathan T Barron, Ravi Ramamoorthi, and Ren Ng. Nerf: Representing scenes as neural radiance fields for view synthesis. *Communications of the ACM*, 65(1):99–106, 2021. 2
- [26] Richard A Newcombe, Shahram Izadi, Otmar Hilliges, David Molyneaux, David Kim, Andrew J Davison, Pushmeet Kohi, Jamie Shotton, Steve Hodges, and Andrew Fitzgibbon. Kinectfusion: Real-time dense surface mapping and tracking. In *2011 10th IEEE international symposium on mixed and augmented reality*, pages 127–136. Ieee, 2011. 8
- [27] Johannes L Schonberger and Jan-Michael Frahm. Structure-from-motion revisited. In *Proceedings of the IEEE conference on computer vision and pattern recognition*, pages 4104–4113, 2016. 2
- [28] Johannes L Schönberger, Enliang Zheng, Jan-Michael Frahm, and Marc Pollefeys. Pixelwise view selection for unstructured multi-view stereo. In *Computer Vision–ECCV 2016: 14th European Conference, Amsterdam, The Netherlands, October 11–14, 2016, Proceedings, Part III 14*, pages 501–518. Springer, 2016. 2
- [29] Matias Turkulainen, Xuqian Ren, Iaroslav Melekhov, Otto Seiskari, Esa Rahtu, and Juho Kannala. Dn-splatter: Depth and normal priors for gaussian splatting and meshing. In *2025 IEEE/CVF Winter Conference on Applications of Computer Vision (WACV)*, pages 2421–2431. IEEE, 2025. 3, 4
- [30] Jiepeng Wang, Yuan Liu, Peng Wang, Cheng Lin, Junhui Hou, Xin Li, Taku Komura, and Wenping Wang. Gaus-surf: Geometry-guided 3d gaussian splatting for surface reconstruction. *arXiv preprint arXiv:2411.19454*, 2024. 2, 3, 6, 7, 8
- [31] Xiangyu Wang, Jingsen Zhu, Qi Ye, Yuchi Huo, Yunlong Ran, Zhihua Zhong, and Jiming Chen. Seal-3d: Interactive pixel-level editing for neural radiance fields. In *Proceedings of the IEEE/CVF International Conference on Computer Vision*, pages 17683–17693, 2023. 3
- [32] Mingqiao Ye, Martin Danelljan, Fisher Yu, and Lei Ke. Gaussian grouping: Segment and edit anything in 3d scenes. In Aleš Leonardis, Elisa Ricci, Stefan Roth, Olga Russakovsky, Torsten Sattler, and Gül Varol, editors, *Computer Vision – ECCV 2024*, pages 162–179, Cham, 2025. Springer Nature Switzerland. 3
- [33] Mulin Yu, Tao Lu, Linning Xu, Lihan Jiang, Yuanbo Xiangli, and Bo Dai. Gsdg: 3dgs meets sdf for improved rendering and reconstruction. *arXiv preprint arXiv:2403.16964*, 2024. 3
- [34] Zehao Yu, Torsten Sattler, and Andreas Geiger. Gaussian opacity fields: Efficient adaptive surface reconstruction in unbounded scenes. *ACM Transactions on Graphics (TOG)*, 43(6):1–13, 2024. 3, 6, 7, 8
- [35] Yu-Jie Yuan, Yang-Tian Sun, Yu-Kun Lai, Yuewen Ma, Rongfei Jia, and Lin Gao. Nerf-editing: Geometry editing of neural radiance fields. In *Proceedings of the IEEE/CVF conference on computer vision and pattern recognition*, pages 18353–18364, 2022. 3
- [36] Matthias Zwicker, Hanspeter Pfister, Jeroen Van Baar, and Markus Gross. Ewa volume splatting. In *Proceedings Visualization, 2001. VIS'01.*, pages 29–538. IEEE, 2001. 3